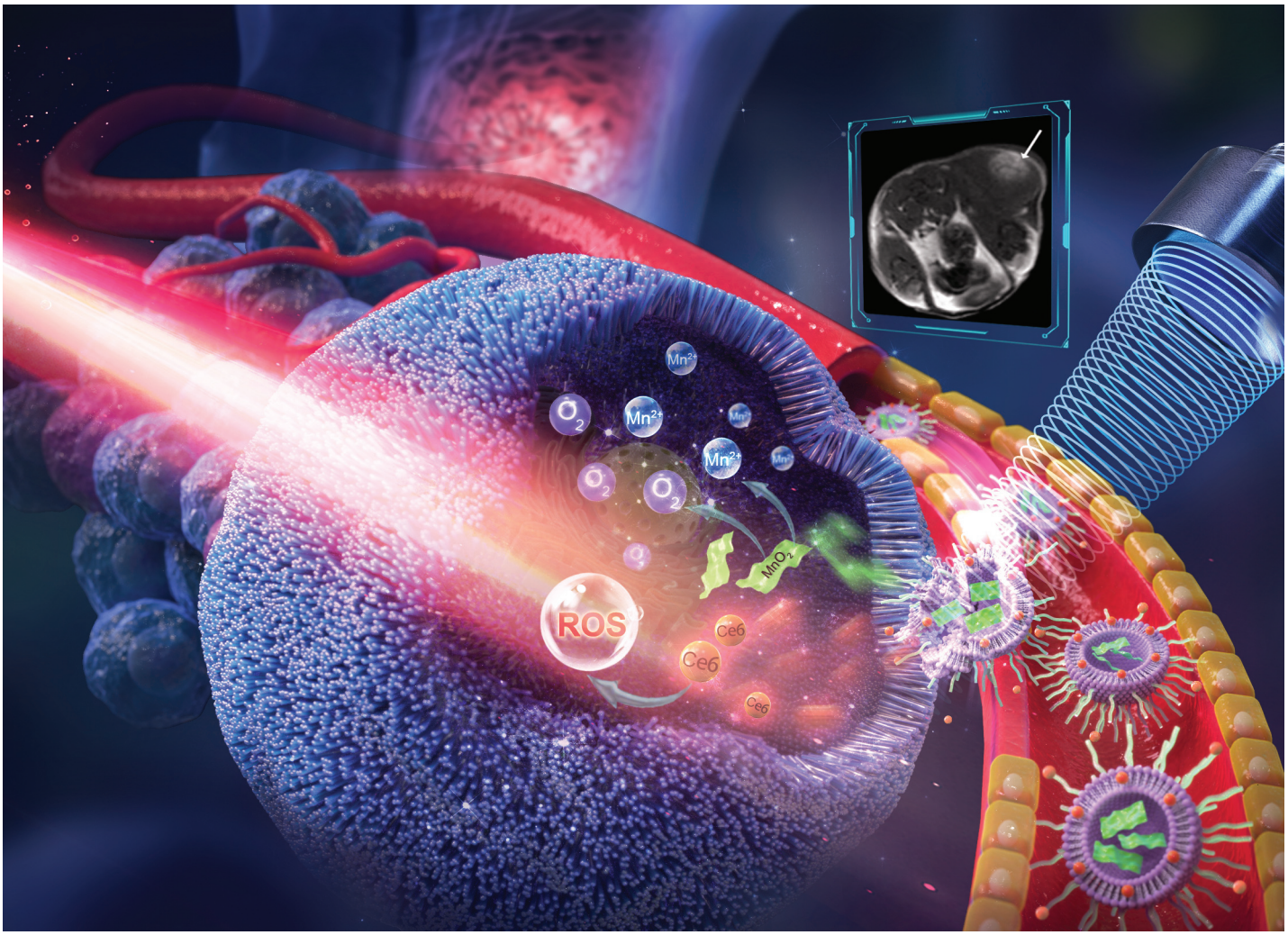

Showcasing research of Prof. Dr. Tingting Zheng, Prof. Dr. Xintao Shuai, Prof. Yun Chen, Prof. Li Liu and Prof. MD. Desheng Sun's Cooperative work from Shenzhen Key Laboratory for Drug Addiction and Medication Safety, Department of Ultrasound, Institute of Ultrasonic Medicine, Peking University Shenzhen Hospital, Shenzhen Peking University-The Hong Kong University of Science and Technology Medical Center, Shenzhen, China.

MnO_2/Ce6 microbubble-mediated hypoxia modulation for enhancing sono-photodynamic therapy against triple negative breast cancer

Here, MnO_2/Ce6 microbubbles associated with ultrasound and magnetic resonance technology were applied to achieve a non-invasive diagnosis and treatment method for malignant tumors in general. We focused on Triple negative breast cancer (TNBC). When ultrasound imaging detected tumor, MnO_2 and Ce6 nanoparticles were targeted released immediately by the cavitation effect of microbubbles. MnO_2 rapidly release Mn^{2+} and O_2 upon encountering H_2O_2 specific to malignant tumors. Mn^{2+} yield in T1-weighted imaging with MRI. Meanwhile, O_2 can improve the oxygen-depleted state of the cancer microenvironment, and activate Ce6> to release reactive oxygen species (ROS) in combination with focused ultrasound (FUS) and/or laser. ROS lyse all biomacromolecular structures in cancer, killing it, which achieves the best effect of photoacoustic dynamic therapy. This study provides a new integrated preclinical theranostics scheme for TNBC treatment.

As featured in:

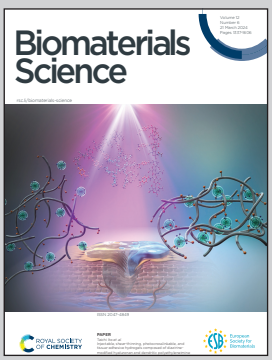

See Li Liu, Yun Chen, Desheng Sun, Xintao Shuai, Tingting Zheng *et al.*, *Biomater. Sci.*, 2024, **12**, 1465.

ROYAL SOCIETY OF CHEMISTRY

rsc.li/biomaterials-science

Registered charity number: 207890

Biomaterials Science

ROYAL SOCIETY OF CHEMISTRY

PAPER

View Article Online
View Journal | View Issue

Cite this: *Biomater. Sci.*, 2024, **12**, 1465

MnO_2/Ce6 microbubble-mediated hypoxia modulation for enhancing sono-photodynamic therapy against triple negative breast cancer†

Ping Li,‡[a] Xiao Tan, ‡[a,b] Qing Dan,‡[a] Azhen Hu,‡[a] Zhengming Hu,‡[a] Xiaoting Yang,[a] Jianhua Bai,[a] Xiaoyu Chen,[a] Bowei Li,[c] Guanxun Cheng,[c] Li Liu,*[a] Yun Chen,*[a] Desheng Sun, *[a] Xintao Shuai *[d] and Tingting Zheng *[a]

Received 17th July 2023,
Accepted 15th January 2024

DOI: 10.1039/d3bm00931a

rsc.li/biomaterials-science

Sono-photodynamic therapy (SPDT) has emerged as a promising treatment modality for triple negative breast cancer (TNBC). However, the hypoxic tumor microenvironment hinders the application of SPDT. Herein, in this study, a multifunctional platform (MnO_2/Ce6@MBs) was designed to address this issue. A sono-photosensitizer (Ce6) and a hypoxia modulator (MnO_2) were loaded into microbubbles and precisely released within tumor tissues under ultrasound irradiation. MnO_2 *in situ* reacted with the excess H_2O_2 and H^+ and produced O_2 within the TNBC tumor, which alleviated hypoxia and augmented SPDT by increasing ROS generation. Meanwhile, the reaction product Mn^{2+} was able to achieve *T*1-weighted MRI for enhanced tumor imaging. Additionally, Ce6 and microbubbles served as a fluorescence imaging contrast agent and a contrast-enhanced ultrasound imaging agent, respectively. In *in vivo* anti-tumor studies, under the FL/US/MR imaging guidance, MnO_2/Ce6@MBs combined with SPDT significantly reversed tumor hypoxia and inhibited tumor growth in 4T1-tumor bearing mice. This work presents a theragnostic system for reversing tumor hypoxia and enhancing TNBC treatment.

1. Introduction

Triple negative breast cancer (TNBC), accounting for 15%–20% of breast cancer, exhibits poor prognosis and lacks efficient therapy strategies.[1–5] Novel treatment modalities are in high demand. Photodynamic therapy (PDT) and sonodynamic therapy (SDT) have emerged as alternative or adjuvant therapy modalities for malignant tumors, including TNBC, due to the non-invasiveness and minimal side effects.[6–10] Based on the administration of a photosensitizer or a sonosensitizer, generally non-toxic when used in appropriate concentrations, PDT or SDT produces toxic singlet oxygen ($^1O_2$) in the presence of oxygen to cause cancer cell death under light or ultrasound (US) irradiation.[11–15] However, the clinical applications of PDT have been limited primarily because of its shallow penetration depth. In contrast, SDT is capable of penetrating deeply into internal tissues and organs. In this scenario, the combination of SDT and PDT, termed sono-photodynamic therapy (SPDT), shows promising potential to overcome the limitations of single modality treatment.[16–25]

The principle of SPDT is using both sound and light to activate a sono-photosensitizer to cause damage to cancer cells, which augments the anti-tumor performance with fewer side effects since cell death may be induced using less exposure to US or light. Additionally, US, combined with microbubbles, remarkably facilitates cell membrane permeability for cellular uptake of sono-photosensitizers, which is well-known as the US targeted microbubble destruction (UTMD) effect, allowing a lower dosage of sono-photosensitizer.[26–32] For example, Ce6, as a second-generation sensitizer, is able to produce toxic $^1O_2$ for anti-cancer treatment under US and laser irradiation. Ce6 does not only work as a sono-photosensitizer, but also serves as a fluorescence (FL) imaging contrast agent for *in vivo* imaging with high resolution and high sensitivity. However, free Ce6 exhibits difficulty in efficiently accumulating into tumour tissues, thus decreasing the therapeutic efficacy of SPDT. Microbubbles, widely accepted as excellent drug car-

[a]*Shenzhen Key Laboratory for Drug Addiction and Medication Safety, Department of Ultrasound, Institute of Ultrasonic Medicine, Peking University Shenzhen Hospital, Shenzhen Peking University-The Hong Kong University of Science and Technology Medical Center, Shenzhen 518036, P.R. China. E-mail: liuli@pkuszh.com, yunchen@sphmc.org, szdssun@163.com, kyzs_018@126.com*
[b]*Zunyi Medical University, Zunyi 563000, P.R. China*
[c]*Department of Medical Imaging, Peking University Shenzhen Hospital, Shenzhen 518036, P.R. China*
[d]*Sun Yat-sen University, Guangzhou 510000, P.R. China. E-mail: shuaixt@mail.sysu.edu.cn*

†Electronic supplementary information (ESI) available: Fig. S1–S6. See DOI: https://doi.org/10.1039/d3bm00931a

‡These authors contributed equally to this work.

riers, can address this issue. In this context, Ce6 is loaded and delivered into tumor regions, and subsequently precisely released *via* UTMD effects when combined with US irradiation.

Furthermore, the hypoxic tumor microenvironment (TME), displaying a low oxygen level, limits the therapeutic outcomes of SPDT.[33–37] The consumption of oxygen during SPDT could further aggravate the oxygen deficiency within tumor sites, resulting in unfavourable outcomes. Many approaches have been applied to improve tumor hypoxia by enhancing the SPDT efficacy. For example, Li *et al.* reported a perfluorocarbon-based "oxygen bomb" PSPP-Au_{980}-D, which could carry and deliver oxygen to tumor sites for enhancing PDT against hypoxic orthotopic pancreatic cancer.[38] Other strategies designed TME-responsive nanostructures, making use of the overexpression of acid and H_2O_2 within tumor sites, to alleviate tumor hypoxia. Sheng and co-workers developed an ultrasmall gold nanozyme that catalyzed the decomposition of H_2O_2 to O_2 within tumor regions to increase TME oxygenation and subsequently enhanced PDT against TNBC.[39,40] Similarly, Shuai and colleagues developed a series of MnO_2-based nanoplatforms which were responsive to H_2O_2/H^+ in the TME, producing oxygen for modulating hypoxia and sequentially promoting PDT.[41] Interestingly, MnO_2 transferred into Mn^{2+}, thus serving as a *T*1-weighted magnetic resonance imaging (MRI) contrast agent for distinguishing tumor tissues and the surrounding normal tissues.

Herein, in this study, we developed a theragnostic strategy for enhanced SPDT against TNBC on the basis of a multifunctional platform (MnO_2/Ce6@MBs). As illustrated in Scheme 1, Ce6 and MnO_2 were loaded into microbubbles and *in situ* released into the tumor region by UTMD. The H_2O_2/pH-responsive MnO_2 nanoparticles then modulated tumor hypoxia by generating O_2, further enhancing the SPDT efficacy of Ce6. In addition, the as-prepared MnO_2/Ce6@MBs, consisting of three crucial imaging contrast agents (Ce6, microbubbles, and Mn^{2+}), allowing FL/US/MR imaging, were able to accurately guide the following therapy procedures. Thus, our proposed TME-responsive and O_2 supplying system showed great potential to realize precise and efficient treatment for TNBC.

2. Experimental section

2.1. Materials

DSPC and DSPE-PEG2000 were purchased from Avanti (USA). MnO_2 nanosheets and Ce6 were obtained from Xi'an Ruixi

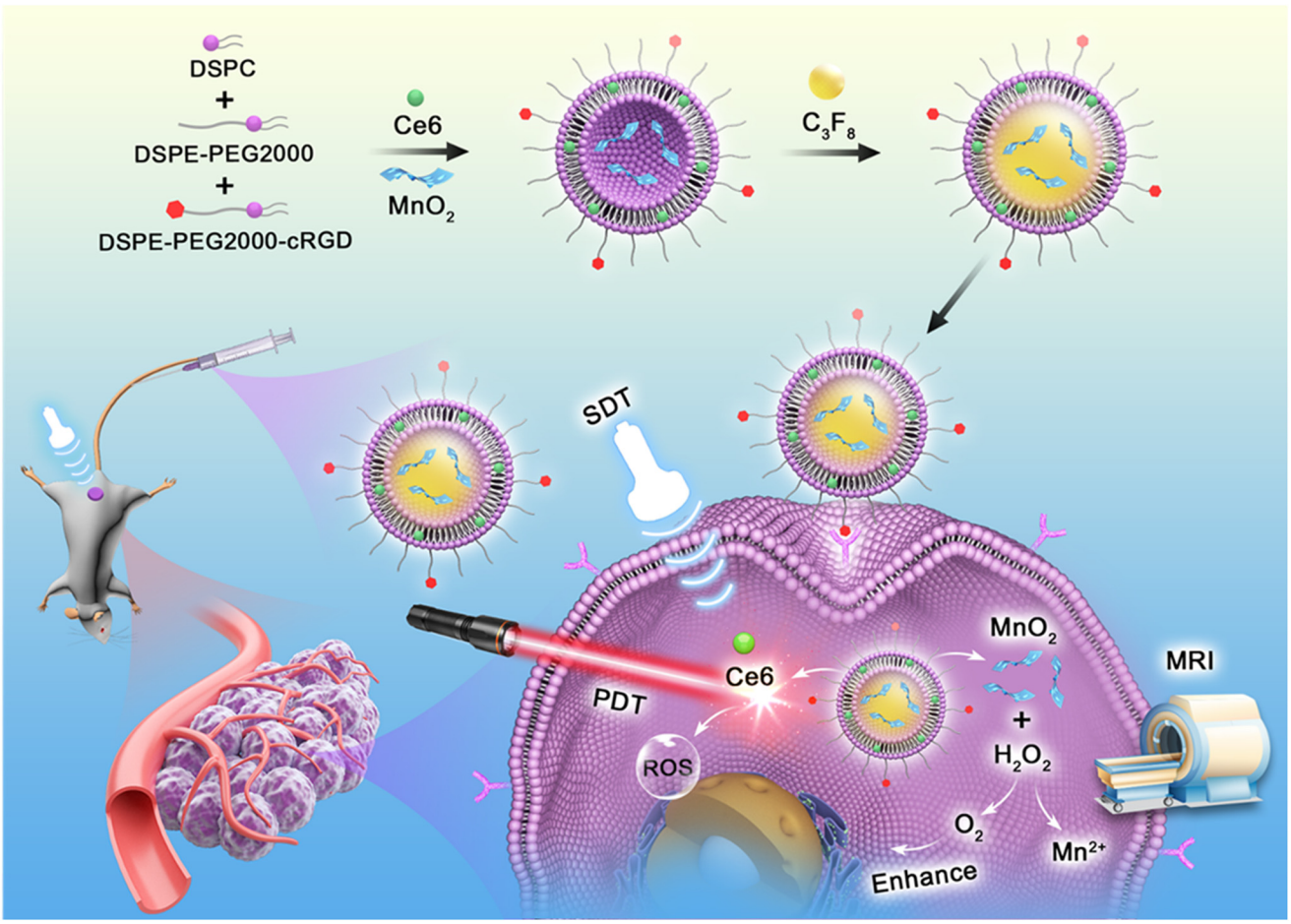

Scheme 1 Schematic illustration of the MnO_2/Ce6@MB-mediated TNBC imaging and treatment.

Biotechnology Co., Ltd (China). The Singlet Oxygen Sensor Green (SOSG) reagent and Annexin V-IF488/PI assay kit were purchased from Thermo Fisher Scientific (USA). The H_2DCFA ROS detection kit was obtained from Invitrogen (USA). The HIF-1α ELISA kit was offered by Shanghai Jianglai Biotechnology Co., Ltd (China).

2.2. Preparation of MnO_2/Ce6@MBs

We prepared MnO_2/Ce6@MBs by the thin film hydration method.[42] Briefly, DSPC and DSPE-PEG2000, weighting 3 mg in total, were dissolved in chloroform (125 μL) at a molar ratio of 18 : 1 : 1, in which Ce6 was incorporated. The mixture was fully dispersed by using an ultrasonic cleaner for 3 min and subsequently transferred to a sterile glass test tube. Under a fume hood, nitrogen was blown for 1 h until the chloroform in the test tube completely evaporated. After being vacuum pumped for 1 h, the complex was added with MnO_2 solution (250 μg mL^{-1}, 1 mL) for ultrasonic hydration, and heated to 60 °C for the lipid phase transition. MnO_2/Ce6@Liposomes were obtained and transferred into vials with perfluoropropane to generate MnO_2/Ce6 microbubbles (MnO_2/Ce6@MBs). The prepared MnO_2/Ce6@MBs were stored in the dark at 4 °C.

2.3. Characterization of MnO_2/Ce6@MBs

The morphology and particle size of MnO_2/Ce6@Liposomes were observed using transmission electron microscopy (TEM, JEM-1400plus, Japan). The morphology of MnO_2/Ce6@MBs was investigated using an FL microscope (80I, Japan). The particle size distribution and zeta potential of MnO_2/Ce6@MBs were measured by dynamic light scattering (DLS) using a zetasizer equipment (Malvern Instruments, UK). The ultraviolet absorption spectrum was detected by using an ultraviolet-visible (UV-Vis) spectrometer (UV-1200, Shanghai Mipuda). The concentration of MnO_2/Ce6@MBs was detected by using a particle counter (PSS, 780-A 7000APS, USA).

2.4. ROS generation of MnO_2/Ce6@MBs

A singlet oxygen ($^1O_2$) probe (SOSG) was employed to determine the *in vitro* $^1O_2$ generation of MnO_2/Ce6@MBs solutions under SPDT treatment. In brief, SOSG agents were added to PBS, MnO_2/Ce6@Liposomes, and MnO_2/Ce6@MBs solutions (at an equivalent desired concentration of Ce6), respectively. The concentration of Ce6 and MnO_2 was 40 μg mL^{-1} and 20 μg mL^{-1}, respectively. US and laser irradiation were subsequently applied for 1 min. The parameters of the ultrasound and laser irradiation were as follows: 1 MHz, 50% duty cycle, 300 mW cm^{-2}; 660 nm, 150 mW cm^{-2}. Then, an FL spectrometer (FLS920, Edinburgh Instruments) was used to determine the FL intensity of SOSG (excitation/emission = 504 nm/525 nm) every 2 min.

For ROS determination at the cellular level, confocal FL microscopy and flow cytometry were employed. There were five groups: (1) control; (2) MnO_2/Ce6@MBs; (3) MnO_2/Ce6@MBs + SDT; (4) MnO_2/Ce6@MBs + PDT; and (5) MnO_2/Ce6@MBs + SPDT. For SDT, the conditions were set as: 1 MHz, 50% duty cycle, 300 mW cm^{-2}, 1 min. For PDT, the conditions were set as: 660 nm, 150 mW cm^{-2}, 1 min. For SPDT, the cell received SDT and PDT in sequence. The concentration of Ce6 and MnO_2 were 40 μg mL^{-1} and 20 μg mL^{-1}, respectively. Of note, all US and laser illumination treatments at the cellular level in this study followed the protocol mentioned above.

Murine 4T1 cells (5×10^4 cells per well) were seeded into an 8-well culture dish overnight. The cells received different treatments and then the H_2DCFA ROS detection reagents were added. After further incubation for 30 min, the cells were washed 3 times with PBS and observed under a confocal microscope (CLSM; LSM719, Carl Zeiss, Jena, Germany).

Likewise, quantitative analysis was performed by flow cytometry. The 4T1 cells were seeded into a 6-well plate at a density of 2×10^5 per well and incubated overnight. After various treatments, ROS reagents were supplemented, and the cells were then incubated for another 30 min. The cells were collected in Eppendorf tubes after washing with PBS, trypsinization, and centrifugation (3000 rpm, 10 min) for flow cytometry assay. The FL signals of H_2DCFA were collected on the FITC channel. Data were analyzed using the FlowJo program.

For ROS determination at the tissue level, 4T1 tumor-bearing mice were randomly divided into five groups: (1) control; (2) MnO_2/Ce6@MBs; (3) MnO_2/Ce6@MBs + SDT; (4) MnO_2/Ce6@MBs + PDT; (5) MnO_2/Ce6@MBs + SPDT. For SDT, the conditions were set as: 1 MHz, 50% duty cycle, 300 mW cm^{-2}, 10 min. For PDT, the conditions were set as: 660 nm, 800 mW cm^{-2}, 10 min. For SPDT, the cells received SDT and PDT in sequence. The dosage of MnO_2/Ce6@MBs was 200 μL with the Ce6 concentration of 500 μg mL^{-1} and the MnO_2 concentration of 250 μg mL^{-1}. In brief, the mice were intravenously injected with MnO_2/Ce6@MBs, followed by the corresponding US and laser treatments. After 24 h, the tumor-bearing mice were intratumorally injected with SOSG reagents (50 μM, 25 μL). Thirty minutes later, iced tumor tissue sections were obtained and observed under an inverted FL microscope.

2.5. *In vitro* anti-tumor effects

2.5.1. Cell uptake of MnO_2/Ce6@MBs. Due to the intrinsic FL signals of Ce6, it can be used as a tracer to visualize the uptake and colocation of MnO_2/Ce6@MBs in cells. The 4T1 cells (5×10^4 cells per well) were seeded into an 8-well culture dish overnight. After different treatments, cells were washed and stained with DAPI, and rhodamine-phalloidin (RP) to visualize the cell nucleus and cytoskeletons. The cells were observed under a confocal microscope.

2.5.2. Cytotoxicity of MnO_2/Ce6@MBs. The CCK-8 method was used to examine the toxicity of MnO_2/Ce6@MBs in 4T1 cells. The 4T1 cells were seeded into 96-well plates and treated with MnO_2/Ce6@MBs of different concentrations (0, 2.5, 5, 10, 20 μg mL^{-1}) after culturing for 24 h. Then, the cells were divided into four groups according to different treatment methods: (1) MnO_2/Ce6@MBs; (2) MnO_2/Ce6@MBs + SDT; (3) MnO_2/Ce6@MBs + PDT; (4) MnO_2/Ce6@MBs + SPDT. After culturing for another 24 h, cell viability was determined by a CCK-8 assay.

2.5.3. Anti-tumor effect of MnO_2/Ce6@MBs + SPDT. The apoptosis analysis of MnO_2/Ce6@MBs + SPDT was investigated *via* flow cytometry. The 4T1 cells were seeded into a 6-well plate at a density of 2×10^5 per well and incubated overnight. After various treatments, Annexin V-FITC/PI reagents were supplemented, and the cells were then incubated for another 30 min. The cells were collected in Eppendorf tubes after washing with PBS, trypsinization, and centrifugation (3000 rpm, 10 min) for flow cytometry assay. Data were analyzed using the FlowJo program.

2.6. *In vivo* imaging

2.6.1. Animal models. BALB/c mice were used to establish the 4T1 tumor-bearing mouse models. All experiments were carried out in accordance with the regulations of the Animal Ethics Committee of Shenzhen Peking University-The Hong Kong University of Science and Technology Medical Center. Tumor volumes (V) were calculated according to $V = (L \times W^2)/2$, where L and W were the longest and widest diameter of the tumor size. When the tumor volume reached about 50 mm^3 and 200 mm^3, the mice were used for therapy and imaging studies, respectively.

2.6.2. FL imaging. Mice were imaged using the IVIS spectrum imaging system (Caliper IVIS Spectrum, IVIS) at various time points (0, 2, 4, 8, 12, 24 h) after intravenous injection with MnO_2/Ce6@MBs. The average FL intensity at the corresponding time point was obtained at the excitation wavelength of 565 nm and the emission wavelength of 694 nm. Qualitative and quantitative analyses were carried out using the Living Image 4.2 software.

2.6.3. US imaging. After intravenous injection with MnO_2/Ce6@MBs (200 μL), gray scale and contrast-enhanced ultrasonography (CEUS) were conducted on an US imaging system (Mindray Resona7, China).

2.6.4. MRI imaging. Tumor-bearing mice were injected with 200 μL of MnO_2/Ce6@MBs and treated with ultrasound irradiation (0.8 MHz, 900 mVpp, 1×10^4 cycles, 10 min) to burst microbubbles and release MnO_2. *T*1-weighted MRI images were obtained at 0, 0.5, 4, and 8 h after administration of MnO_2/Ce6@MBs. The experimental parameters for the T1 fast recovery spin-echo sequence were set as follows: repetition time = 600 ms, echo time = 10 ms, slice thickness = 1.5 mm, resolution = 1.5 × 1.0 × 2.0 mm, and field of view = 49 × 49 mm^2.

2.7. *In vivo* anti-tumor effects

4T1 tumor-bearing mice were randomly divided into five groups: (1) control; (2) MnO_2/Ce6@MBs; (3) MnO_2/Ce6@MBs + SDT; (4) MnO_2/Ce6@MBs + PDT; and (5) MnO_2/Ce6@MBs + SPDT. The dosage of MnO_2/Ce6@MBs was 200 μL with the Ce6 concentration of 500 μg mL^{-1} and the MnO_2 concentration of 250 μg mL^{-1}. The conditions for SDT were set as: 0.8 MHz, 900 mVpp, 1×10^4 cycles, and 10 min. The conditions for PDT were set as: 660 nm, 800 mW cm^{-2}, 10 min. For SPDT, the cell received SDT and PDT in sequence. Mice received different treatments on the 2nd, 4th, 6th, 8th, 10th, and 12th day. Every two days, the tumor volumes and body weights were recorded. On the 14th day post-treatment, the main organs, including the heart, liver, spleen, lungs, and kidneys, and tumor tissues from mice were collected for hematoxylin and eosin (H&E) staining and Ki67 staining

The liver and kidney function indicators, including alanine aminotransferase (ALT), aspartate aminotransferase (AST), and blood urea nitrogen (BUN), were analyzed. For hypoxia modulation studies, RT-qPCR, western blotting and ELISA were used to evaluate HIF-1α. The specific primers for RT-qPCR experiments were ACAAGTCACCACAGGACAG (HIF-1α-F) and AGGGAGAAAATCAAGTCG (HIF-1α-R).

2.8. Statistical analysis

The data were presented as the mean ± standard deviation. The statistical significance was evaluated by a two-tailed Student's *t*-test or one-way analysis of variance. $p < 0.05$ was considered as statistically significant.

3. Results and discussion

3.1. Synthesis and characterization of MnO_2/Ce6@MBs

MnO_2/Ce6@MBs with suitable particle sizes and uniform dispersion were successfully prepared by the thin film hydration method.[42] The TEM image showed that the MnO_2/Ce6@Liposomes had spherical structures with an average size of approximately 200 nm (Fig. 1A). The morphology of MnO_2/Ce6@MBs observed by FL imaging showed that the MnO_2/Ce6@MBs had uniform dispersion, spherical structures, and red rims due to the intrinsic FL signal of Ce6 (Fig. 1B), which enabled MnO_2/Ce6@MBs to serve as an FL contrast agent for *in vitro* and *in vivo* visualization studies. The mean hydrodynamic size of MnO_2/Ce6@MBs was about 2.3 μm with the polydispersity index of 0.12, which was in the range of a typical microbubble size, allowing further biomedical applications. The zeta potential of MnO_2/Ce6@MBs was about −31 mV. The encapsulation efficiency and loading content of Ce6 were about 95.30% ± 1.63% and 9.53 wt% ± 0.13 wt%, respectively. Similarly, the encapsulation efficiency and loading content of MnO_2 were about 73.8% ± 1.45% and 3.69 wt% ± 0.32 wt%, respectively. The concentration of MnO_2/Ce6@MBs was 5×10^8 mL^{-1} determined by using a particle counter. Additionally, the size and concentration stability of MnO_2/Ce6@MBs were investigated. The results showed that MnO_2/Ce6@MBs had a stable mean size of about 2 μm and the mean concentration of 3×10^8 within 24 hours (Fig. S1†), which allowed further *in vivo* imaging and therapy studies of MnO_2/Ce6@MBs.

The $^1O_2$ generation capability of MnO_2/Ce6@MBs was studied using a SOSG agent. PBS, MnO_2/Ce6@Liposomes, and MnO_2/Ce6@MBs received SPDT treatment and their $^1O_2$ generation were determined. As shown in Fig. 1E and F, the SOSG FL intensity of MnO_2/Ce6@Liposomes was lower than that of MnO_2/Ce6@MBs, which was due to higher Ce6 release from microbubbles than liposomes by US irradiation. We also found that with MnO_2/Ce6@MBs could produce higher $^1O_2$ with mul-

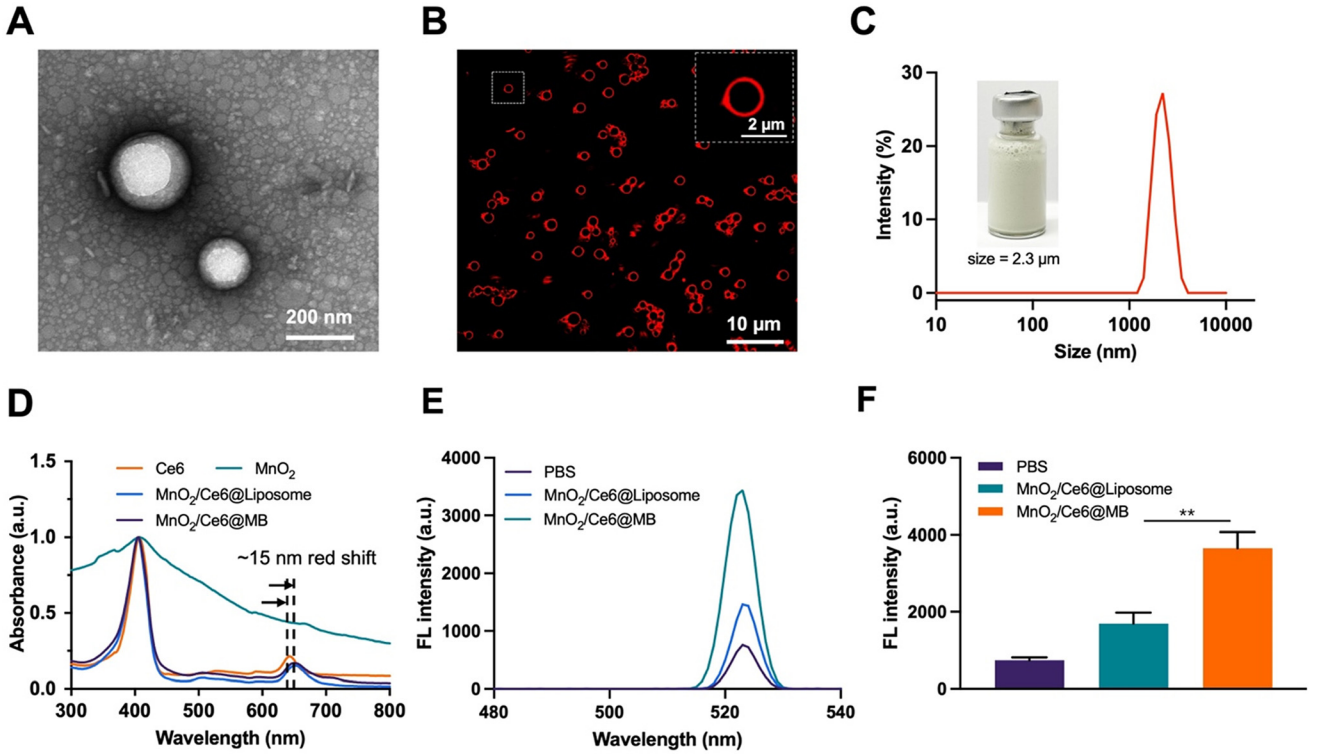

Fig. 1 Characterization of MnO_2/Ce6@MBs. (A) Representative TEM images of MnO_2/Ce6@Liposomes. (B) FL image of MnO_2/Ce6@MBs. Amplified view of a typical MnO_2/Ce6@MBs shown in the inset image (white rectangle with a dashed line). (C) Hydrodynamic size of MnO_2/Ce6@MBs. Digital photo of the MnO_2/Ce6@MBs shown in the inset image. (D) UV-Vis spectra of the free Ce6, MnO_2/Ce6@Liposomes and MnO_2/Ce6@MBs. (E) *In vitro* $^1O_2$ generation of the PBS, MnO_2/Ce6@Liposomes and MnO_2/Ce6@MBs post SPDT treatment. (F) Quantification of (E). $^{**}p < 0.01$.

tiple irradiation processes. MnO_2/Ce6@MBs were exposed to SPDT treatment every two minutes and were tested by using an FL spectra instrument. No obvious SOSG FL intensity changes were observed in PBS solution for 14 min, whereas the SOSG FL intensity rapidly increased in MnO_2/Ce6@Liposomes and MnO_2/Ce6@MBs solutions within 4 min. Then, gradual decreases occurred after 4 min (Fig. S2†). These results suggested that multiple doses of MnO_2/Ce6@MBs + SPDT might present an improved anti-tumor efficacy.

3.2. *In vitro* anti-tumor effects

We firstly evaluated the ROS generation ability of MnO_2/Ce6@MBs at the cellular level. Murine TNBC 4T1 cells were divided into five groups: (1) control; (2) MnO_2/Ce6@MBs; (3) MnO_2/Ce6@MBs + SDT; (4) MnO_2/Ce6@MBs + PDT; (5) MnO_2/Ce6@MBs + SPDT.

A H_2DCFDA ROS detection assay kit was applied for flow cytometry analysis. It showed that the control group and MnO_2/Ce6@MBs group exhibited a very weak ROS FL intensity, which was the physical ROS level in tumor cells. The 4T1 cells treated with MnO_2/Ce6@MBs + SDT, MnO_2/Ce6@MBs + PDT, and MnO_2/Ce6@MBs + SPDT displayed increasing ROS levels, with that of MnO_2/Ce6@MBs + SPDT significantly higher than those of MnO_2/Ce6@MB + SDT and MnO_2/Ce6@MB + PDT (Fig. 2A and B).

Visualization of ROS generation in 4T1 cells and 4T1-tumor tissues were achieved by FL imaging. As shown in Fig. 2C–F, MnO_2/Ce6@MBs + SPDT exhibited most ROS generation compared with that produced by solely SDT or PDT, suggesting that the combination of SDT and PDT was beneficial for enhancing ROS generation and further improving cell killing effects.

We subsequently investigated colocalization and cell uptake of MnO_2/Ce6@MBs making use of the intrinsic red FL of Ce6. Using a multiple staining assay, including the cell nucleus and cytoskeletons, we found that Ce6 was localized in the cell nucleus. Post various treatments, the 4T1 cells were observed under a confocal microscope. No FL signals of Ce6 were found in the control group, while there were weak Ce6 FL signals in the cells incubated with MnO_2/Ce6@MBs. The Ce6 FL signals increased in MnO_2/Ce6@MBs + PDT, which might be caused by the mild thermal effect from laser irradiation. More interestingly, MnO_2/Ce6@MBs + SDT significantly enhanced the cell uptake of MnO_2/Ce6@MBs (Fig. 3A and Fig. S3†). This is due to the UTMD effect that promotes the release of Ce6 from MnO_2/Ce6@MBs as well as 4T1 cell membrane permeation. Eventually, combining US and laser irradiation, 4T1 cells exhibited strongest FL signals of Ce6, which demonstrated the optimal cell uptake of MnO_2/Ce6@MBs, allowing further anti-tumor investigations.

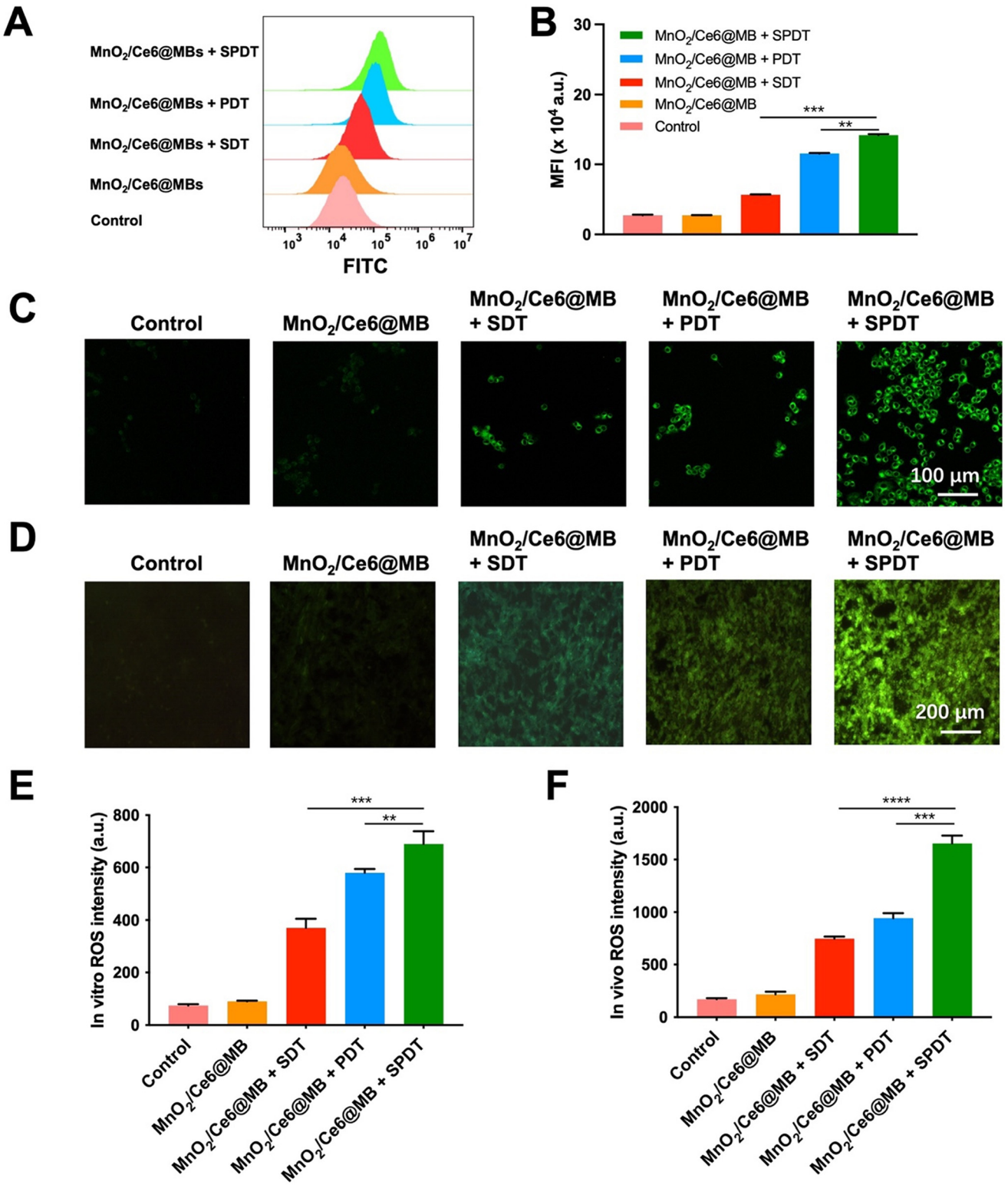

Fig. 2 ROS generation of MnO_2/Ce6@MBs *in vitro* and *ex vivo*. (A) Flow cytometry assay of ROS generation in 4T1 cells after the different treatments. (B) Mean fluorescence intensity (MFI) of (A). (C) Confocal images of ROS in 4T1 cells post various treatments. (D) Confocal images of ROS in the tumor tissues from 4T1-tumor bearing mice post various treatments. (E) Semi-quantificaiton of (C) using ImageJ software. (F) Semi-quantificaiton of (D) using ImageJ software. $^{**}p < 0.01$, $^{***}p < 0.001$ and $^{****}p < 0.0001$.

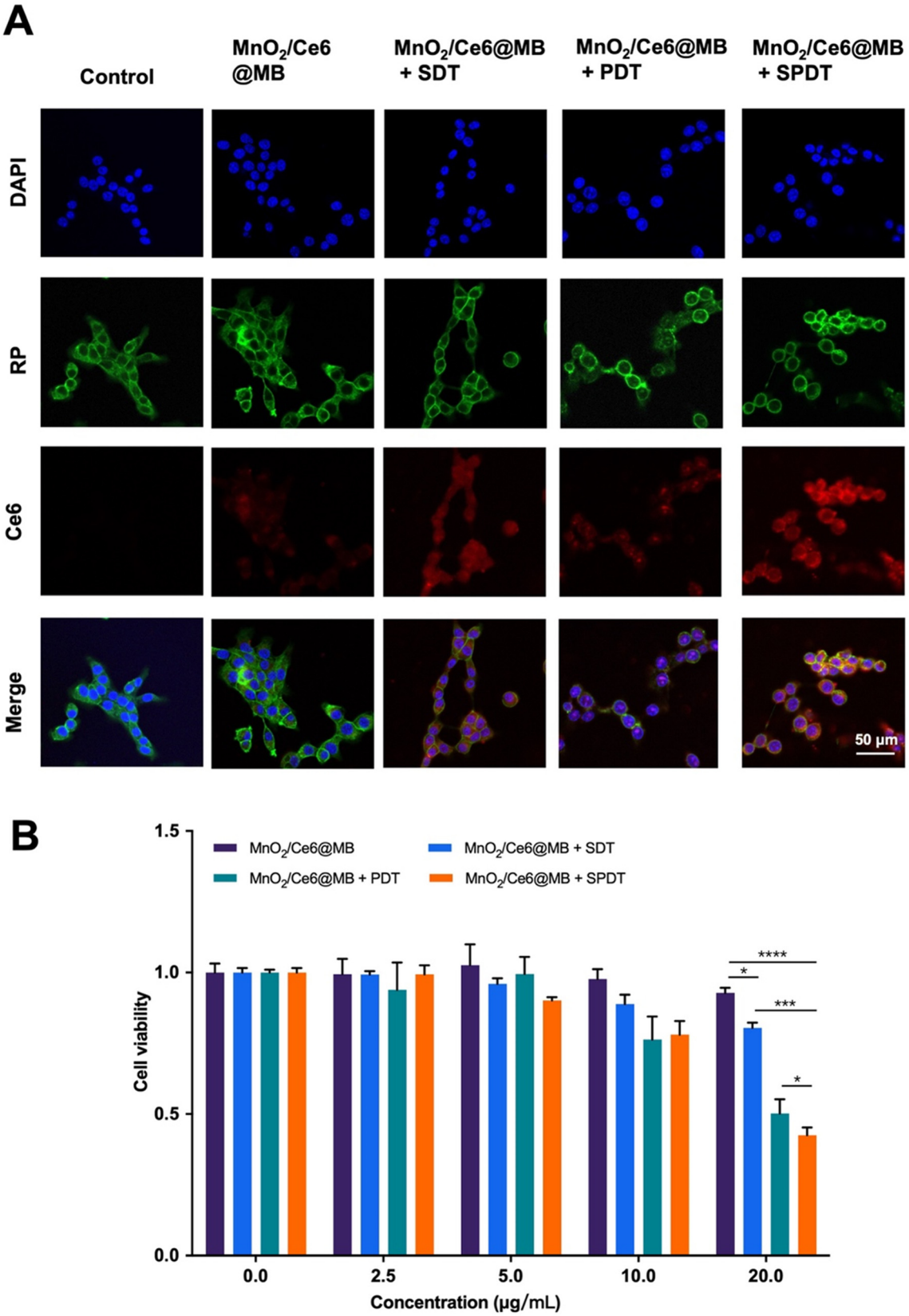

Fig. 3 Cell uptake and cytotoxicity of MnO_2/Ce6@MBs. (A) Confocal FL imaging of 4T1 cells after the various treatments. (B) Cell viability under the different treatments. *$p < 0.05$, ***$p < 0.001$ and ****$p < 0.0001$.

Based on the synergistic effect of SPDT to produce toxic ROS, we verified the cancer cell killing capability of MnO_2/Ce6@MBs + SPDT. We firstly identified the optimal concentration of MnO_2/Ce6@MBs used for *in vitro* studies. Different concentrations of MnO_2/Ce6@MBs (Ce6 concentration: 0 μg mL^{-1}, 2.5 μg mL^{-1}, 5 μg mL^{-1}, 10 μg mL^{-1}, 20 μg mL^{-1}) were incubated with 4T1 cells. Cell viability was determined after SDT, PDT, and SPDT were applied on 4T1 cells, respectively. It showed that MnO_2/Ce6@MBs were biocompatible when 4T1 cells treated with MnO_2/Ce6@MBs of concentration below 20 μg mL^{-1}. However, MnO_2/Ce6@MBs (>20 μg mL^{-1}) combined with SDT exhibited slightly cytotoxicity. MnO_2/Ce6@MBs (20 μg mL^{-1}) + PDT caused about 50% cell death. In contrast, SPDT augmented a cell killing effect compared to SDT or PDT, with cell viability decreasing to about 40% (Fig. 3B). When the Ce6 concentration climbed up to above 20 μg mL^{-1}, it showed negligible cytotoxicity towards 4T1 cells. Hence, the concentration of Ce6 (20 μg mL^{-1}) was chosen for *in vitro* anti-tumor effect studies. Of note, at the cellular level, penetration depth was not a limitation for PDT, thus the assistance with SDT did not play a great role in enhancing PDT.

Flow cytometry was additionally used to analyze the apoptosis of 4T1 cells induced by MnO_2/Ce6@MBs combined with SPDT. After incubation with MnO_2/Ce6@MBs (20 μg mL^{-1}) and then treatment with SDT, PDT, or SPDT, the total apoptosis, including early and late apoptosis, was analysed. In Fig. 4A and B, MnO_2/Ce6@MBs + SPDT presented the apoptosis rate of above 35% compared to MnO_2/Ce6@MBs + SDT (13%) and MnO_2/Ce6@MBs + PDT (16%). We also found the MnO_2/Ce6@MB-mediated SPDT damage cells in a concentration-dependent manner (Fig. 4B), which suggested that with more Ce6 taken up by 4T1 cells and accumulating within tumor tissues, the anti-tumor ability would improve. The outcomes supported our hypothesis that with the assistance of SDT, mainly due to the UTMD effect, the cancer cell killing capability of PDT got significantly enhanced by improving targeted drug release, cell membrane permeation, and cell uptake. It showed that the synergistic therapy strategy would provide satisfactory outcomes in further *in vivo* studies.

3.3. Multimodal imaging *in vivo*

The key elements, Ce6, microbubbles, and Mn^{2+}, in MnO_2/Ce6@MBs, were supposed to enhance multimodal imaging. Ce6 is an FL imaging contrast agent and microbubbles were usually applied for contrast-enhanced US (CEUS) imaging. In addition, in the tumor microenvironment, the acid (H^+) reacts with MnO_2 to produce Mn^{2+} for enhanced MRI imaging. Herein, we first evaluated the *in vivo* multimodal imaging performance of MnO_2/Ce6@MBs with FL imaging, US imaging, and MRI.

The tumor accumulation and metabolism of MnO_2/Ce6@MBs were visualized using a small animal *in vivo* FL imaging system. Fig. 5A shows that after the intravenous injection of MnO_2/Ce6@MBs into TNBC tumor-bearing mice, FL images of the whole mouse body were obtained at 0, 2, 4, 8,

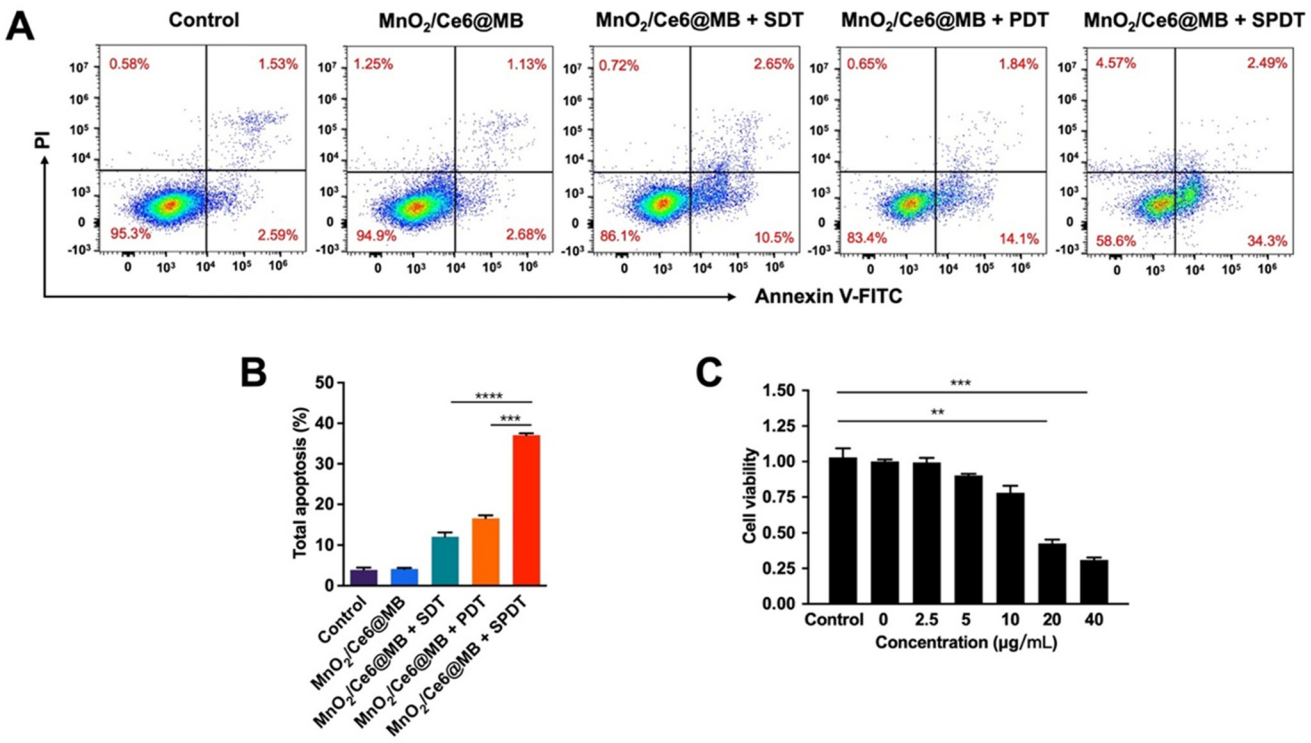

Fig. 4 *In vitro* anti-tumor effect of MnO_2/Ce6@MBs. (A) 4T1 cell apoptosis assay by flow cytometry after the different treatments. (B) Quantification of (A). (C) Evaluation of the cell killing effects of MnO_2/Ce6@MBs + SPDT *via* the CCK-8 assay. $^{**}p < 0.01$, $^{***}p < 0.001$ and $^{****}p < 0.0001$.

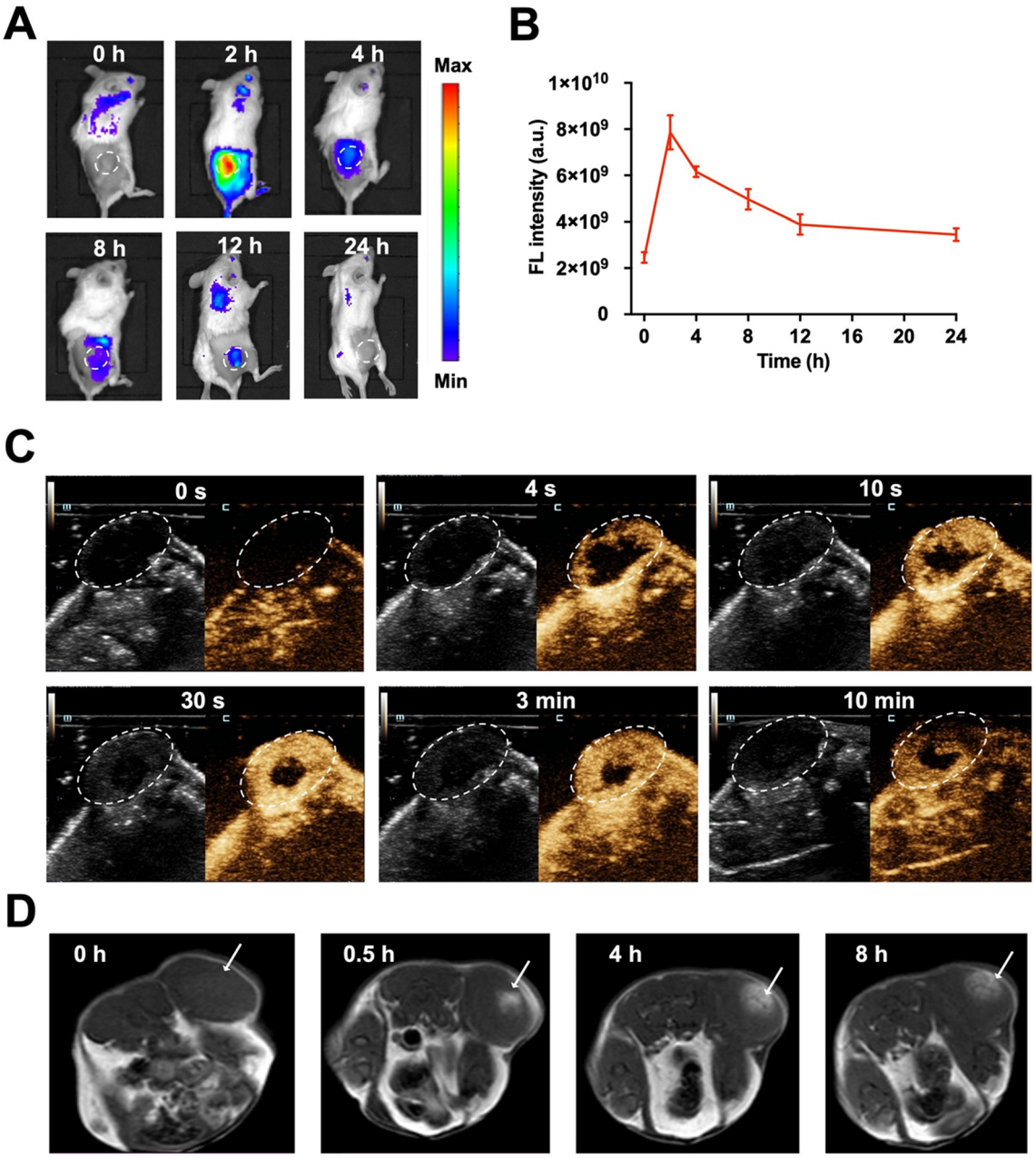

Fig. 5 *In vivo* multimodal imaging. (A) FL imaging in 4T1 tumor-bearing mice at preset time points post intravenous injection of MnO_2/Ce6@MBs. Tumors are shown within the white dashed line. (B) Semi-quantificaiton of (A). (C) US imaging on B mode and CEUS mode for 4T1 tumors (white dashed line) after injection of MnO_2/Ce6@MBs. (D) *T*1-weighted MRI images of the 4T1 tumor (white arrow) at various time points after the administration of MnO_2/Ce6@MBs.

12, and 24 h. Obviously, MnO_2/Ce6@MBs reached within tumor sites at 2 h, with the peak tumor accumulation about 4-fold higher compared to that at 0 h. The FL intensity signals of MnO_2/Ce6@MBs within tumor tissues then gradually decreased starting from 4 h post injection of MnO_2/Ce6@MBs. It also demonstrated that MnO_2/Ce6@MBs were mainly metabolized *via* the lungs with the peak accumulation at 12 h, which is the typical metabolic pathway of microbubbles (Fig. 5B). At 24 h after injection, the FL signals of MnO_2/Ce6@MBs nearly went down back to the background signal, indicating that within 24 h, the MnO_2/Ce6@MBs were cleared out from the bodies.

We further examined the US imaging capability of MnO_2/Ce6@MBs on both brightness mode (B mode) and CEUS mode. As expected, CEUS was remarkably superior to the B mode for US perfusion imaging. In the 4th second after the intravenous injection of MnO_2/Ce6@MBs, the contour of tumor was distinctly visualized in the CEUS mode. The

enhancement intensity reached the peak value in the 30th second and then gradually decreased starting from the 3rd min. The tumor was clearly imaged until the 10th min (Fig. 5C). The results exhibited the desirable retention and imaging-enhancing abilities of MnO_2/Ce6@MBs, showing its potential for serving as a novel CEUS agent.

Since the tumor microenvironment is mildly acidic, primarily attributed to hypoxia and increased lactate levels in cancer cells, it offered a physical "reaction chamber" for the degradation of MnO_2. MnO_2 interacted with H_2O_2 and H^+ within the tumor, decomposing into Mn^{2+}, which presented high T1 relaxivity in MRI. As shown in Fig. 5D, at 0.5 h post administration of MnO_2/Ce6@MBs, the T1 MRI signals of the tumor were strengthened, significantly distinct from muscle tissues. At 4 h post-injection, the tumor region showed a climax on the MRI signal, which was evidently higher than that in the pre-injection tumor. At 8 h post-injection, the tumor signal in T1 MRI decreased, similar to that at 0.5 h, showing that Mn^{2+} was gradually removed out *via* blood circulation. Thus, MnO_2/Ce6@MBs being H_2O_2-/pH-degradable had great potential for enhancing cancer MRI imaging, supplementary to FL imaging and CEUS imaging.

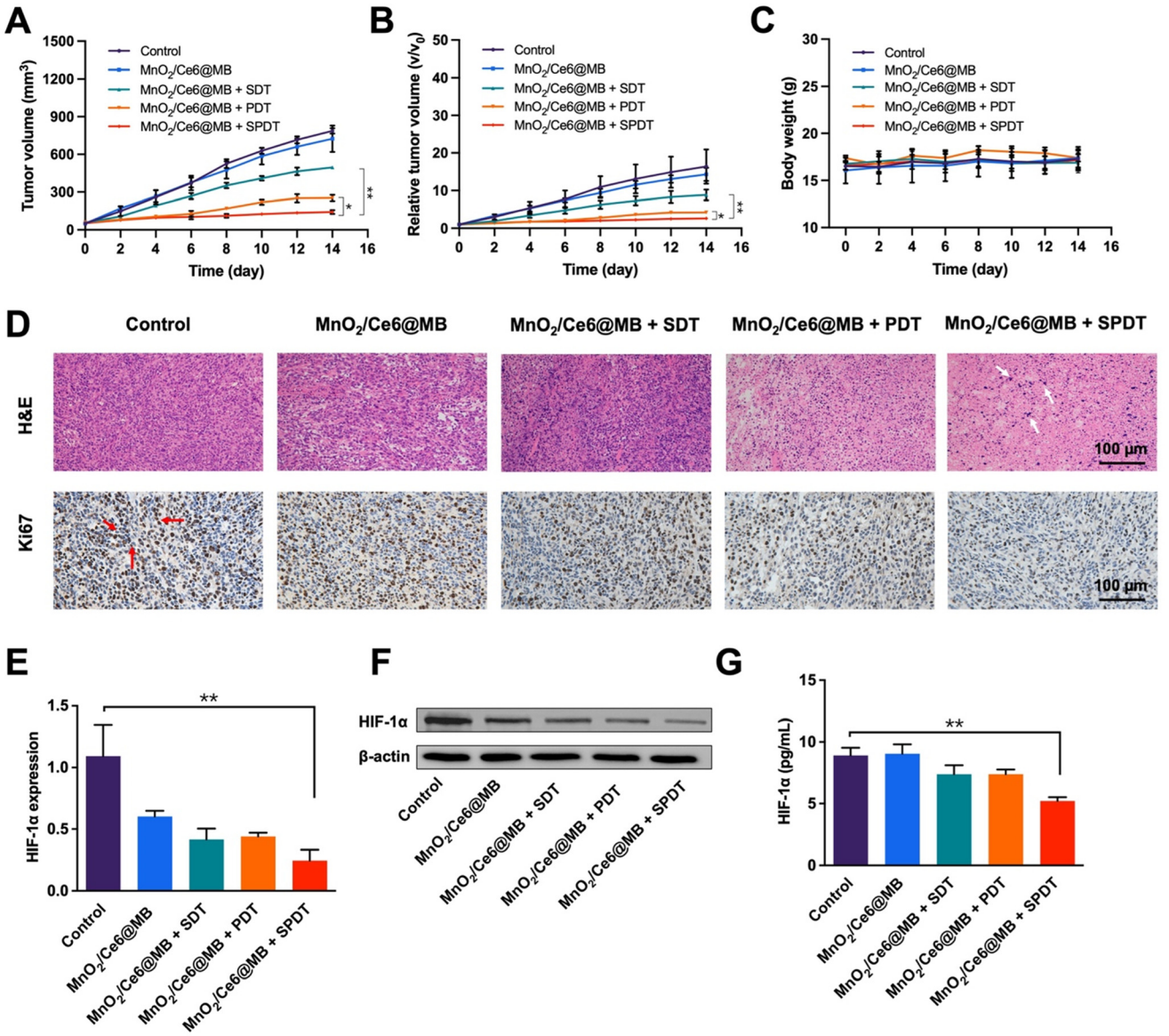

Fig. 6 *In vivo* anti-tumor effects. (A) 4T1 tumor growth curve with time after the different treatments. (B) Tumor volume changes with time after the different treatments. (C) Body weights of 4T1-tumor bearing mice. (D) Histological images of tumor tissues that underwent various treatments. In the H&E assay, tumor apoptosis and necrosis are indicated by white arrows. In Ki67 staining, tumor proliferation is indicated by red arrows. (E) RT-qPCR analysis of the HIF-1α gene expression. (F) Western blot assay of the HIF-1α protein. (G) ELISA assay of the HIF-1α protein. *$p < 0.05$ and **$p < 0.001$.

3.4. Anti-tumor effect *in vivo*

Inspired by the remarkable tumor accumulation and ROS generation capability of MnO_2/Ce6@MBs, we conducted tumor growth inhibition studies to evaluate the *in vivo* anti-cancer performance of MnO_2/Ce6@MBs. Tumor-bearing mice were randomly divided into five groups (n = 6): (1) control; (2) MnO_2/Ce6@MBs; (3) MnO_2/Ce6@MBs + SDT; (4) MnO_2/Ce6@MBs + PDT; (5) MnO_2/Ce6@MBs + SPDT.

The mice were injected with PBS in the control group and MnO_2/Ce6@MBs in the other four groups, followed by SDT, PDT, and SPDT. Tumor sizes and body weights were recorded every two days. The tumors of the control group and MnO_2/Ce6@MBs group grew rapidly as expected. In contrast, the tumor sizes were suppressed in the mice that received MnO_2/Ce6@MBs combined with SDT, PDT, and SPDT. MnO_2/Ce6@MBs + SPDT presented the most satisfactory therapeutic outcomes among all treatments (Fig. 6A). On the 14th day of the treatments, the mean tumor volume was about 140 mm^3 in the MnO_2/Ce6@MBs + SPDT group compared to that in the control group (about 780 mm^3). In tumor size change analysis, we found that the tumors increased by about 2.68-, 4.21-, 8.84-, 14.31-, and 16.39-fold, respectively, in the corresponding groups on the 14th day compared to those in the pre-treated mice (Fig. 6B).

During the period of treatments, the body weights of the mice were recorded. No apparent body loss was observed in all mice. Additionally, the H&E staining of the main organs, including the heart, liver, spleen, lungs and kidneys, showed no apparent histological changes in all mice after 14 days (Fig. S4†). Furthermore, the AST, ALT and BUN as liver and renal function indicators were also examined, without abnormal changes after various treatments (Fig. S5†).

The mechanism of the cancer killing effect was analyzed by multiple methods. Histological studies of tumor tissues demonstrated that there was obvious cell damage in H&E staining, such as cell apoptosis and necrosis, in the MnO_2/Ce6@MBs + SPDT group, while the Ki67 index was much lower in the MnO_2/Ce6@MBs + SPDT group compared to the other four groups, indicating less cancer cell proliferation (Fig. 6D). Hypoxia modulation was further investigated at genetic and protein levels. HIF-1α is an important indicator for assessing tissue hypoxia. The expression of the HIF-1α gene was determined by the RT-qPCR method. It was found that after the MnO_2/Ce6@MBs + SPDT treatment, the HIF-1α expression reversed markedly compared to the control group. Notably, the MnO_2/Ce6@MBs itself could also improve tumor hypoxia to some extent (Fig. 6E). The protein levels of HIF-1α were further evaluated by western blotting and ELISA. Accordingly, the HIF-1α protein significantly decreased in the MnO_2/Ce6@MBs + SPDT group (Fig. 6F and G and Fig. S6†). These results demonstrated that the prepared MnO_2/Ce6@MBs were able to generate sufficient toxic $^1O_2$ under SPDT treatment to cause cancer cell death *via* hypoxia environment regulation.

4. Conclusions

In summary, we successfully developed a multifunctional theragnostic platform for enhancing precise TNBC treatment. The as-prepared MnO_2/Ce6@MBs, consisting of three crucial imaging contrast agents (Mn^{2+}, Ce6, and microbubbles), showed high-performance imaging function for FL/MR/US imaging and were able to guide the following therapy procedures. Microbubbles combined with US, as drug "missiles", precisely delivered the sono-photosensitizer (Ce6) to the tumor "nests" for efficient treatment. Additionally, the MnO_2 nanoparticles were tumor microenvironment (H_2O_2/pH)-responsive, modulating tumor hypoxia to enhance SPDT. This study provides a promising platform for the imaging and therapy of TNBC.

Ethical statement

All procedures were approved by the Animal Use and Care Committee of Shenzhen Peking University-The Hong Kong University of Science and Technology Medical Center (SPHMC) with the NIH Guidelines for the Care and Use of Laboratory Animals and Public Health Policy (protocol number 2020-032).

Author contributions

Manuscript drafting, data curation, investigation, and visualization: Ping Li, Xiao Tan, and Qing Dan; methodology, validation, and project administration: Azhen Hu and Zhengming Hu; *in vitro* experiments: Azhen Hu, Xiaoting Yang and Jianhua Bai; *in vivo* imaging experiments: Xiaoyu Chen, Bowei Li, and Guanxun Cheng; *in vivo* anti-cancer experiments: Ping Li, Xiao Tan, and Qing Dan; study design and conceptualization: Tingting Zheng and Xintao Shuai; resources and funding acquisition: Li Liu, Yun Chen, Zhengming Hu and Tingting Zheng; supervision and manuscript editing: Desheng Sun and Zhengming Hu. All authors have approved the manuscript and agree with its submission to *Biomaterials Science*.

Conflicts of interest

The authors have no conflicts to declare.

Acknowledgements

This work was supported by the Natural Science Foundation of Guangdong Province (2022A1515010296, 2022A1515010986), the Science and Technology Project of Shenzhen (JCYJ20200109140212277, JCYJ20210324110211031, JCYJ20210324131402008, KXCFZ202002011010487), the Shenzhen Key Medical Discipline Construction Fund (SZXK051), and the Sanming Project of Medicine in Shenzhen (SZSM202111011). We appreciate all the work Yulin Ye, Die

Hu, and Xiaoxin He have done to help us conduct the animal experiments.

References

1 H. Sung, J. Ferlay, R. L. Siegel, M. Laversanne, I. Soerjomataram, A. Jemal and F. Bray, *Ca-Cancer J. Clin.*, 2021, **71**, 209–249.
2 P. Zagami and L. A. Carey, *npj Breast Cancerr*, 2022, **8**, 95.
3 K.-S. Parham, C.-G. L. Luis and A. S. Maria Inmaculada, *Breast J.*, 2019, DOI: **10.1111/tbj.13369**.
4 A.-M. S. Sumayah, S. J. Justin, G. Olga B and M. T. Tamara, *Drug Delivery Transl. Res.*, 2018, DOI: **10.1007/s13346-018-0551-3**.
5 S. Ma, Y. Zhao, W. C. Lee, L.-T. Ong, P. L. Lee, Z. Jiang, G. Oguz, Z. Niu, M. Liu, J. Y. Goh, W. Wang, M. A. Bustos, S. Ehmsen, A. Ramasamy, D. S. B. Hoon, H. J. Ditzel, E. Y. Tan, Q. Chen and Q. Yu, *Nat. Commun.*, 2022, **13**, 4118.
6 Z. Zeng, C. Zhang, J. Li, D. Cui, Y. Jiang and K. Pu, *Adv. Mater.*, 2021, **33**, e2007247.
7 M. Yang, T. Yang and C. Mao, *Angew. Chem., Int. Ed.*, 2019, **58**, 14066–14080.
8 M. Wysocki, B. Czarczynska-Goslinska, D. Ziental, M. Michalak, E. Güzel and L. Sobotta, *ChemMedChem*, 2022, **17**, e202200185.
9 S. Son, J. H. Kim, X. Wang, C. Zhang, S. A. Yoon, J. Shin, A. Sharma, M. H. Lee, L. Cheng, J. Wu and J. S. Kim, *Chem. Soc. Rev.*, 2020, **49**, 3244–3261.
10 Um Wooram, E. K. Pramod Kumar, L. Jeongjin, K. Chan Ho, Y. Dong Gil and P. Jae Hyung, *Chem. Commun.*, 2021, **57**, 2854–2866, DOI: **10.1039/d0cc07750j**.
11 A. P. McHale, J. F. Callan, N. Nomikou, C. Fowley and B. Callan, *Adv. Exp. Med. Biol.*, 2016, **880**, 429–450.
12 M. Xu, L. Zhou, L. Zheng, Q. Zhou, K. Liu, Y. Mao and S. Song, *Cancer Lett.*, 2021, **497**, 229–242.
13 P. Sarbadhikary, B. P. George and H. Abrahamse, *Theranostics*, 2021, **11**, 9054–9088.
14 J. H. Correia, J. A. Rodrigues, S. Pimenta, T. Dong and Z. Yang, *Pharmaceutics*, 2021, **13**, 1332.
15 Z. Gong and Z. Dai, *Adv. Sci.*, 2021, **8**, 2002178.
16 P. Wang, C. Li, X. Wang, W. Xiong, X. Feng, Q. Liu, A. W. Leung and C. Xu, *Ultrason. Sonochem.*, 2015, **23**, 116–127.
17 D. Sun, Z. Zhang, M. Chen, Y. Zhang, J. Amagat, S. Kang, Y. Zheng, B. Hu and M. Chen, *ACS Appl. Mater. Interfaces*, 2020, **12**, 40728–40739.
18 H. Wang, J. Shang, F. Yang, S. Zhang, J. Cui, X. Hou, Y. Li, W. Liu, X. Shu, Y. Liu and B. Sun, *Photodiagn. Photodyn. Ther.*, 2023, **42**, 103642.
19 Y. Yang, J. Tu, D. Yang, J. L. Raymond, R. A. Roy and D. Zhang, *Curr. Pharm. Des.*, 2019, **25**, 401–412.
20 Y. Zheng, J. Ye, Z. Li, H. Chen and Y. Gao, *Acta Pharm. Sin. B*, 2021, **11**, 2197–2219.
21 L. Liu, J. Zhang, R. An, Q. Xue, X. Cheng, Y. Hu, Z. Huang, L. Wu, W. Zeng, Y. Miao, J. Li, Y. Zhou, H.-Y. Chen, H. Liu and D. Ye, *Angew. Chem., Int. Ed.*, 2023, **62**, e202217055.
22 K. C. Sadanala, P. K. Chaturvedi, Y. M. Seo, J. M. Kim, Y. S. Jo, Y. K. Lee and W. S. Ahn, *Anticancer Res.*, 2014, **34**, 4657–4664.
23 X. Wang, W. Zhang, Z. Xu, Y. Luo, D. Mitchell and R. W. Moss, *Integr. Cancer Ther.*, 2009, **8**, 283–287.
24 B. M. Borah, J. Cacaccio, F. A. Durrani, W. Bshara, S. G. Turowski, J. A. Spernyak and R. K. Pandey, *Sci. Rep.*, 2020, **10**, 21791.
25 Q. Li, Q. Liu, P. Wang, X. Feng, H. Wang and X. Wang, *Ultrasonics*, 2014, **54**, 981–989.
26 Y. Wu, T. Sun, J. Tang, Y. Liu and F. Li, *Ultrasound Med. Biol.*, 2020, **46**(3), DOI: **10.1016/j.ultrasmedbio.2019.09.017**.
27 T. Benjamin, B. Maike, O. Tarun, M. Diana, V. Seena Koyadan, S. Julia, B. Louis, S. Gert, K. Fabian and L. Twan, *J. Controlled Release*, 2016, **23**, 77–85.
28 Y. Tian, Z. Liu, H. Tan, J. Hou, X. Wen, F. Yang and W. Cheng, *Int. J. Nanomed.*, 2020, 1178–2013.
29 G. Fan, J. Qin, X. Fu, X. Si, L. Li, K. Yang, B. Wang, H. Lou and J. Zhu, *Front. Oncol.*, 2022, **12**, DOI: **10.3389/fonc.2022.823956**.
30 C. B. Walton, C. D. Anderson, R. Boulay and R. V. Shohet, *J. Visualized Exp.*, 2011, **52**, 2963.
31 I. Lentacker, I. De Cock, R. Deckers, S. De Smedt and M. Moonen, *Adv. Drug Delivery Rev.*, 2014, **72**, 49–64.
32 J. Deprez, G. Lajoinie, Y. Engelen, S. De Smedt and I. Lentacker, *Adv. Drug Delivery Rev.*, 2021, **172**, 9–36.
33 K. Graham and E. Unger, *Indian J. Nephrol.*, 2018, **13**, 6049–6058.
34 X. Jing, F. Yang, C. Shao, K. Wei, M. Xie, H. Shen and Y. Shu, *Mol. Cancer*, 2019, **18**, 157.
35 W. R. Wilson and M. P. Hay, *Nat. Rev. Cancer*, 2011, **11**, 393–410.
36 P. Vaupel, *Oncologist*, 2004, **9**, 10–17.
37 M. Hockel and P. Vaupel, *JNCI, J. Natl. Cancer Inst.*, 2001, **93**, 266–276.
38 S. Zhang, Z. Li and Q. Wang, *Adv. Mater.*, 2022, **34**(29), e2201978.
39 Q. Dan, D. Hu, Y. Ge, S. Zhang, S. Li, D. Gao, W. Luo, T. Ma, X. Liu, H. Zheng, Y. Li and Z. Sheng, *Biomater. Sci.*, 2020, **8**, 973–987.
40 Q. Dan, Z. Yuan, S. Zheng, H. Ma, W. Luo, L. Zhang, N. Su, D. Hu, Z. Sheng and Y. Li, *Pharmaceutics*, 2022, **14**, 1645.
41 M. Yu, X. Duan, Y. Cai, F. Zhang, S. Jiang, S. Han, J. Shen and X. Shuai, *Adv. Sci.*, 2019, **6**, 1900037.
42 V. Daeichin, T. van Rooij, I. Skachkov, B. Ergin, P. A. C. Specht, A. Lima, C. Ince, J. G. Bosch, A. F. W. van der Steen, N. de Jong and K. Kooiman, *IEEE Trans. Ultrason. Ferroelectr. Freq. Control*, 2017, **64**, 555–567.